



# Carbon nanodots/WO<sub>3</sub> nanorods Z-scheme composites: Remarkably enhanced photocatalytic performance under broad spectrum

Jun Zhang<sup>a</sup>, Yue Ma<sup>a</sup>, Yilin Du<sup>a</sup>, Huizhong Jiang<sup>a</sup>, Dandan Zhou<sup>b</sup>, Shuangshi Dong<sup>a,\*</sup>

<sup>a</sup> Key Laboratory of Groundwater Resources and Environment, Ministry of Education, Jilin University, Changchun, 130021, Jilin, China

<sup>b</sup> School of Environment, Northeast Normal University, Changchun 130117, Jilin, China



## ARTICLE INFO

### Article history:

Received 7 January 2017

Received in revised form 28 February 2017

Accepted 2 March 2017

Available online 6 March 2017

### Keywords:

Carbon nanodots/WO<sub>3</sub> nanorods

Photocatalytic

UV-vis-NIR light

Interfacial charge transfer

Z-scheme

## ABSTRACT

The search for low-cost, earth-abundant and environmentally friendly photocatalysts that can efficiently function over the entire UV-vis-NIR spectrum remains one of the most pressing challenges in the photocatalytic elimination of pollutants from water. Herein, we accurately designed and fabricated a direct Z-scheme carbon nanodots/WO<sub>3</sub> nanorods composite (CDots/WO<sub>3</sub>) with highly enhanced photo-response and broad-spectrum photocatalytic activity. Under ultraviolet, visible, near-infrared (UV, Vis, NIR) irradiation, respectively, the removal efficiencies of rhodamine B (RhB) always decreased in the order CDots/WO<sub>3</sub> (97.1, 99.1, 61.2%) > prepared WO<sub>3</sub> nanorods (66.6, 69.1, 22.4%) > commercial WO<sub>3</sub> nanoparticles (22.1, 11.6, ~0%). Additionally, reaction rate constants of 0.4030 and 0.2889 h<sup>-1</sup> were achieved by the CDots/WO<sub>3</sub> nanocomposites when photo-oxidizing tetracycline hydrochloride (TCH) and phenol, respectively, both of which were ~2.9 times higher than those for WO<sub>3</sub> nanorods. This excellent photocatalytic performance was ascribed to synergistic effects, including the highly dispersed carbon nanodots on the surface of the WO<sub>3</sub> nanorods and efficient charge separation induced by the heterostructure formed between carbon nanodots and WO<sub>3</sub> nanorods. Accordingly, a mechanism was proposed to account for the photocatalytic reaction process. The prepared catalyst showed no obvious change in its photocatalytic performance or other chemical properties after 5 cycles of use. Therefore, the carbon nanodots/WO<sub>3</sub> nanocomposites may represent a new strategy for the full-spectrum utilization of solar light, providing an invaluable methodology for the remediation of current water-pollution issues.

© 2017 Elsevier B.V. All rights reserved.

## 1. Introduction

Efficient semiconductor photocatalysis is a promising and effective strategy for purifying water contaminated by various environmental pollutants [1]. To date, a wide variety of semiconductor materials have been developed, including ZnO, TiO<sub>2</sub>, C<sub>3</sub>N<sub>4</sub>, Bi<sub>2</sub>WO<sub>6</sub>, CdS and Ag<sub>2</sub>O, among others [2–6]. However, two key factors seriously restrict the further application of these photocatalysts, namely, the low solar-light utilization efficiency and rapid electron-hole recombination [7]. Therefore, numerous efforts have been made to solve these problems.

Regarding solar-energy utilization, the preparation of semiconductor photocatalysts that can harvest the entire spectrum of solar light, from ultraviolet (UV) to near-infrared (NIR) wavelengths, while achieving efficient solar-energy conversion, remains one of the most important challenges [6,8]. Recently, several UV-vis-NIR-

active catalysts have been reported, including CdS, Ag<sub>2</sub>O, BiOI and carbon nanodots (CDots) [4,6,9–11]. Among them, CDots, a new member of the carbon family consisting of particles with sizes below 10 nm, have attracted increasing interest because of unique properties including their large two-photon absorption cross sections, up-conversion ability, low toxicity, high biocompatibility and excellent electron-transfer and electron-reservoir properties [12,13]. Accordingly, CDots can be employed as a co-catalyst to build surface separation centers for electrons and reduce the recombination rate of charge carriers. It has been reported that CDots/TiO<sub>2</sub> nanotube arrays [14], CDots/Ag<sub>3</sub>PO<sub>4</sub> [15], CDots/H- $\gamma$ -TaON [8], CDots/BiOX (X = Cl, Br and I) [16], CDots/Bi<sub>2</sub>WO<sub>6</sub> [5] and CDots/g-C<sub>3</sub>N<sub>4</sub> [12] composites as well as CDots/CdS [17] heterostructures exhibit enhanced photocatalytic activity and structural stability, compared with single-species catalysts, for the photo-decomposition of organic compounds, evolution of hydrogen by water splitting or solar-light-driven conversion of CO<sub>2</sub> to methanol. The conjugated  $\pi$  structure of the CDots in these composites plays an important role in their improved photocatalytic activities [8]. Therefore, CDots could potentially function as a co-

\* Corresponding author.

E-mail address: [dongshuangshi@gmail.com](mailto:dongshuangshi@gmail.com) (S. Dong).

catalyst, capable of harnessing a broader range of visible or NIR light to enhance the performance of the main photocatalysts.

Recently, one-dimensionally (1-D) nanostructured semiconductor photocatalysts have received extensive attention, and are considered to be ideal photocatalytic materials because their reduced grain boundaries can shorten the transmission path of the photo-generated charges and realize the effective separation of electron–hole pairs [18–21]. Their high crystallinity and abundance of surface active sites are conducive to photo-absorption and redox reactions, and allow them to efficiently gather organic pollutants in wastewater [20,22]. Considering the above-mentioned properties and previous reports regarding 1-D nanomaterials, it is likely that they have the potential to achieve higher photocatalytic activity than nanoparticles.

Among the wide range of 1-D nanostructured semiconductors, tungsten oxide ( $WO_3$ ) nanorods have been regarded as particularly suitable candidates because of their stable physicochemical properties, resilience to photo-corrosion effects, relatively narrow band-gap energy (2.4–2.8 eV) and the high oxidative power of their valence band (VB) holes [20,23]. In addition, in contrast with  $WO_3$  nanoparticles,  $WO_3$  nanorods, with their high specific surface area, provide more active sites and attachment points, which is conducive to the formation of composite photocatalysts. In spite of these advantages, the photocatalytic activity of  $WO_3$  nanorods alone is still limited by several critical drawbacks. First, their intrinsic band-gap energy (2.4–2.8 eV) severely limits their solar-light utilization efficiency [23]. Second, they usually suffer from a high recombination rate of the charge carriers at the surface, which are slow to participate in interface redox reactions [20]. Last, their relatively low conduction band (CB) level does not provide a sufficient potential to react with strong electron acceptors, which directly results in fast recombination and thus lower photocatalytic activity. Therefore, considerable efforts have been devoted to the development of a novel  $WO_3$  nanorods-based photocatalyst that can efficiently utilize a wide spectrum of solar-light irradiation.

It has already been confirmed that CDots can efficiently enhance the photocatalytic and photo-electrochemical performance of  $WO_3$  under visible-light irradiation [24,25]. Shi et al. [24] showed that a CDots/ $WO_3$  electrode had a higher photo-current and photo-electric conversion efficiency than the corresponding  $WO_3$  electrode. Yang et al. used  $IO_3^-/I^-$  as a shuttle redox mediator to transfer the photo-generated electrons in the CB of  $WO_3$  to the VB of CDots, and found that this Z-scheme was an effective strategy to improve the photocatalytic performance of  $WO_3$  [25]. Thus, on the basis of these reports, it is plausible that the CDots/ $WO_3$  nanorods Z-scheme heterostructure could be used as an efficient photocatalyst. However, little is known about the photocatalytic activity and mechanism of CDots/ $WO_3$  nanocomposites over the UV–vis–NIR broad spectrum. Is a direct Z-scheme system still present in CDots/ $WO_3$  in the absence of redox mediators such as  $IO_3^-/I^-$ ? It is desirable to construct direct Z-scheme systems from CDots/ $WO_3$  nanorods composites to enhance the photo-response and broad-spectrum photocatalytic performance of  $WO_3$ , and to reveal the corresponding photocatalytic oxidation mechanisms accurately and in detail.

To the best of our knowledge, there is no previous report of simultaneous broad-spectrum light utilization and efficient charge separation by a system comprising CDots coupled with  $WO_3$  nanorods to form an all-solid-state direct Z-scheme heterojunction. Herein, for the first time, we synthesized UV-, visible- and NIR-light-driven CDots/ $WO_3$  nanorods composite photocatalysts, ensuring the fast interior transport, surface separation and effective solar-light absorption of the carriers so as to enhance the photocatalytic activity. The  $WO_3$  nanorods were used as a supporting material, leading to the homogeneous dispersion of the

prepared CDots nanoparticles on the nanorod surfaces to form CDots/ $WO_3$  nanorods Z-scheme heterostructures with spectrum-versatile activity, i.e., UV, visible and NIR. The photocatalytic performance of the catalysts was evaluated by decomposing Rhodamine B (RhB), tetracycline hydrochloride (TCH) and phenol in aqueous solutions under UV, visible and NIR irradiation, respectively. The composites exhibited superior photocatalytic activity, which was mainly ascribed to the synergistic effect between  $WO_3$  nanorods and CDots. Subsequently, a possible photocatalytic mechanism for the broad-solar-spectrum activity of the CDots/ $WO_3$  nanorods heterostructures was proposed. Hence, this work may be of interest to both materials scientists and those working in the area of catalyst design.

## 2. Experimental

### 2.1. Catalysts preparation

All chemicals were analytical grade without further purification. A common electrochemical method was used to synthesize CDots.  $WO_3$  nanorods was prepared via a simple hydrothermal method that according to previous reports with some modified [26]. The detailed processes can be found in Supplementary materials.

CDots/ $WO_3$  nanorods composites prepared via an oil bath reflux. First, 0.1 g  $WO_3$  nanorods dissolved into 80 mL CDots aqueous solution to form a homogeneous mixture. Then, the mixture was transferred to oil bath pot and run at 90 °C for 3 h and the heterostructure was obtained. Last, the resulted samples were washed with ultrapure water for 3 times and dried at 60 °C. For comparison, a series of CDots/ $WO_3$  nanocomposites were prepared by adding different content of CDots (wt%), which were accordingly denoted as X wt% CDots/ $WO_3$  (X = 0.2, 0.4, 0.8 and 1.2). In this paper, we used CDots/ $WO_3$  instead of 0.8 wt% CDots/ $WO_3$ , as it was proved to possess the highest photocatalytic activity and was most intensively studied.

### 2.2. Characterization

The morphology and crystal structure of prepared samples were investigated via the Scanning Electron Microscopy (SEM, JEOL JSM-7001F), Transmission Electron Microscopy (TEM), and High-Resolution TEM (HRTEM) (via a 200 kV FEI-Tecnai F20, USA) measurements. Accordingly, the corresponding 2D fast Fourier transform (FFT) pattern was obtained via Digital Micrograph. The XRD patterns were acquired with a powder X-ray diffraction (XRD, Bruker D8, Germany) equipped with Cu K $\alpha$  radiation. X-ray photo-electron spectroscopy (XPS) was conducted via an X-ray photo-electron spectroscopy using an Al K $\alpha$  ( $h = 1486.6$  eV) radiation excitation source. All of the obtained spectra were calibrated against the C 1s signal at BE = 284.6 eV. The UV–vis–NIR diffuse reflection spectra (DRS) was taken on a Lambda 750 spectrophotometer (Perking Elmer). Raman spectra was obtained by using an HR 800 Raman spectroscope (Horiba Jobin Yvon, France). The Fourier transform infrared (FT-IR) spectrums were investigated by a FT-IR spectrometer (Spectrum One, Perkin Elmer). The photoluminescence (PL) spectra were carried out on a luminescence spectrometer (Cary Eclipse, Varian Medical Systems, USA). The electron spin resonance (ESR) spectra were performed on a Bruker model ESR JES-FA200 spectrometer by using the spin-trap reagent DMPO (5,5-dimethyl-1-pyrroline N-oxide, Sigma Chemical Co.) in water (for hydroxyl radical) and methanol (for superoxide radical).

### 2.3. Photocatalytic measurements

The light source for photocatalytic reaction was a 150 W Xenon lamp (CEL-HXF 300, Beijing Education Au-light Co., Ltd.). Three

different filter glasses were used to allow the pass-through of UV (320–400 nm, UV light reflection filter: CEL-UVREF), visible (420–780 nm, UV–IR cut-off filter: CEL-UVIRCUT420-780) and NIR light ( $\lambda > 780$  nm, IR filter: VISCUT780), respectively (the spectrum and output power of UV, visible and NIR light were shown in Fig. S1 and Table S1). The photocatalytic activity of the as-prepared catalysts under UV, visible and NIR light irradiation were estimated by measuring the degradation rate of RhB ( $10 \text{ mg L}^{-1}$ ) in an aqueous solution. Moreover, phenol ( $20 \text{ mg L}^{-1}$ ) and TCH ( $20 \text{ mg L}^{-1}$ ) were also used as additional target pollutants to eliminate the effect of dye-photo-sensitization. 25 mg photocatalyst were added in a sealed quartz reactor which contained 50 mL aqueous solution with target pollutants. Prior to irradiation, the suspension was magnetically stirred to ensure achieved the adsorption-desorption equilibrium after dark reaction for 60 min. In the process of irradiation, a given volume of suspension was sampled at a certain interval, then was centrifuged immediately to obtain the supernatant for pollutant detection. The reusability and stability of the photocatalysts was measured via repeating the identical experiment for five more times. For comparison, CDots, commercial  $\text{WO}_3$  nanoparticles, and prepared  $\text{WO}_3$  nanorods were used as photocatalytic references under the same experimental conditions.

In the scavenger quenching experiments, the scavengers used was sodium chromate (VI) (0.05 mM, Sigma, 99.5%) for electron, 2,2,6,6-Tetramethyl-1-piperidinyloxy (TEMPO) for  $\cdot\text{O}_2^-$  (1 mM, Sigma, 99%), isopropanol (0.5 mM, Sigma) for  $\cdot\text{OH}$  and sodium oxalate (0.5 mM, Sigma, 99.5%) for hole. The volume ratio of each scavenger and RhB solution was 1:100 in this experiment. Then, the scavengers were added in to the 50 mL RhB ( $10 \text{ mg L}^{-1}$ ) solution before photo-irradiation. After the reaction, the concentrations of RhB were measured. To show a clear comparison, the reaction time for  $\text{WO}_3$  and CDots/ $\text{WO}_3$  were 260 and 160 min, respectively, in this experiment.

The concentration of RhB was determined by an UV-vis spectrophotometer according to its absorbance at 554 nm. The TCH concentration was determined by an Agilent 1100 HPLC equipped with a  $4.6 \times 250$  mm,  $5 \mu\text{m}$  Venusil HILIC column, and the wavelength of the UV detector was set at 356 nm. The mobile phase (v/v) consisted of 0.02 M acetic acid (90%) and acetonitrile (10%) at a flow rate of  $1.0 \text{ mL min}^{-1}$ . The phenol concentration was determined by an Agilent 1100 HPLC equipped with a reverse-phase column (Agilent Eclipse XDB-C18) with 150 mm length and 4.6 mm internal diameter, and the wavelength of the UV detector was set at 270 nm. The mobile phase (v/v) consisted of deionized doubly distilled water (90%) and acetonitrile (10%) at a flow rate of  $1.0 \text{ mL min}^{-1}$ . Besides, the dissolved organic carbon (DOC) of phenol was carried out by a total organic carbon analyzer (SSM-5000A, Shimadzu Company). Below, both of the DOC and phenol/TCH removals were based on mass removals ( $\text{mg L}^{-1}$ ).

#### 2.4. Electrochemical analysis

The transient photo-current measurements and electrochemical impedance spectroscopy (EIS) were performed on CHI-660e electrochemical workstation (Shanghai Chenhua, China) using a three-electrode configuration and the as-prepared samples as working electrode. The working electrodes were prepared by dip-coating method. 5 mg of the sample was suspended in 5 mL of anhydrous ethanol to produce suspension, which was then spin-coated (2000 rpm) onto a FTO glass electrode. The visible light source is a 150 W Xenon lamp with a cutoff filter ( $780 > \lambda > 420$  nm). A solution containing 0.1 M  $\text{Na}_2\text{SO}_4$  aqueous solution was used as the electrolyte.

### 3. Results and discussion

#### 3.1. Characterization of as-prepared materials

The TEM and HRTEM images showed that the prepared CDots presented an irregular spherical shape (Figs. 1 a and S2A). As seen from the particle-size-distribution histogram (embedded in Fig. 1a), the particle diameters ranged from 2.5 to 5.5 nm with an average diameter of 3.7 nm. The HRTEM image of the CDots (Fig. 1a inset) displayed an obvious lattice fringe with a lattice spacing of 0.321 nm, which corresponded well to the (002) crystal plane of graphitic carbon [5]. Consistently with this, the corresponding 2D fast Fourier transform (FFT) pattern (Fig. S2B) exhibited the hexagonal crystalline structure of the CDots, further indicating their successful synthesis. Meanwhile, another lattice fringe, that of graphene, was also observed (see Fig. S2C) [12], indicating that the prepared CDots had formed from the aggregation of graphite fragments.

The SEM (Fig. 1b) and TEM (Fig. 1c) images of the as-prepared CDots/ $\text{WO}_3$  nanocomposite confirmed that the  $\text{WO}_3$  nanorods had a highly ordered, 1-D rod-like structure, with a uniform distribution of the CDots on their surfaces. The HRTEM images (Figs. 1 d and S3C) and FFT patterns (Fig. S3D–F) further confirmed that the CDots and  $\text{WO}_3$  nanorods were strongly bound and in close contact, which we attribute to the formation of C–O bonds between them [24]. This intimate contact between the CDots and  $\text{WO}_3$  nanorods was presumably beneficial to electron transfer from  $\text{WO}_3$  to CDots during photo-excitation, resulting in the reduced probability of electron–hole recombination and the enhanced photocatalytic performance. The HRTEM images also clearly revealed lattice fringes with spacings of 0.370 nm in the nanorods and 0.321 nm in the nanoparticles, which corresponded well to the (020) plane of hexagonal wurtzite-type  $\text{WO}_3$  [20,27] and to the (002) spacing of graphitic carbon [5]. Further details of the morphology of the prepared  $\text{WO}_3$  nanorods and CDots/ $\text{WO}_3$  are given in Fig. S3.

XRD, Raman, FT-IR and XPS analysis were used to characterize the composition and structure of the prepared materials. As shown in Fig. 2a, the XRD patterns of the CDots reflects three prominent peaks. Among them, the peak at  $26^\circ$  was corresponding to the (002) planes of graphite, and the other two peaks emerged at  $22.59^\circ$  and  $18.20^\circ$  were referring to the amorphous carbon and (103) planes (belongs to hexagonal carbon) [28]. The results indicated the transformation of crystalline graphite into amorphous structure carbon, and the partial conversion of  $\text{sp}^2$ -hybridized  $\text{C}=\text{C}$  in the aromatic ring into  $\text{sp}^3$ -hybridized  $\text{C}=\text{C}$  in the CDots [28]. Meanwhile, strong XRD diffraction peaks indicated that the  $\text{WO}_3$  nanorods and CDots/ $\text{WO}_3$  were highly crystalline (Fig. 2a), with the structure of the hexagonal wurtzite phase (JCPDS file no. 75-2187) [26]. No diffraction peaks for the CDots could be observed in the sample of CDots/ $\text{WO}_3$  because of their low content, relatively low diffraction intensity and fine particle size (shown in Fig. 2a) [29]. In addition, there was no obvious difference between the XRD patterns of  $\text{WO}_3$  and CDots/ $\text{WO}_3$ , demonstrating that the presence of CDots negligibly influenced the growth of the nanorods, and that the CDots were only deposited on the surfaces of the  $\text{WO}_3$  nanorods rather than entering into the crystal lattice of  $\text{WO}_3$ . Furthermore, all the peak intensities slightly decreased as the CDots content was increased from 0.2 to 1.2 wt% (Figs. 2 a and S4). This decrease possibly occurred because the increased amounts of CDots on the surfaces of the  $\text{WO}_3$  nanorods blocked the X-ray irradiation and prevented coherent scattering [29]. When varying the concentration of CDots in the CDots/ $\text{WO}_3$  nanocomposites (Fig. S4), no XRD peak shift was observed, which further indicated that the photocatalysts consisted solely of CDots and  $\text{WO}_3$  with no impurities.

In the FT-IR spectrum of the CDots (Fig. 2b), carboxyl, carbonyl and hydroxyl groups can be observed, implying the presence

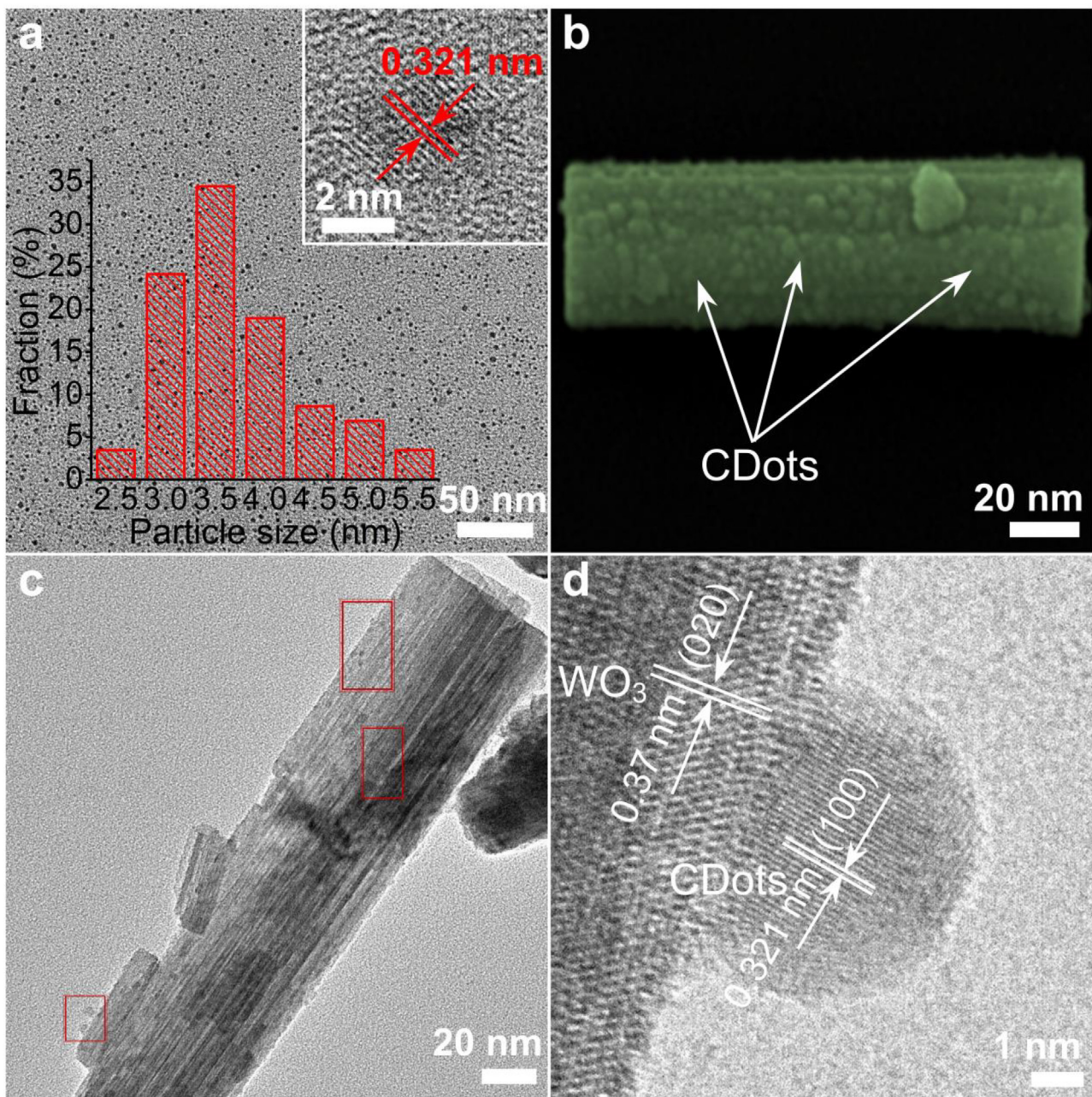


**Fig. 1.** (a) TEM and HRTEM images with size distribution of CDots. Inset is the size distribution analyzed from multiple images. (b) SEM image of as-prepared CDots/WO<sub>3</sub>. TEM (c) and HRTEM (d) images of the CDots/WO<sub>3</sub>. Some representative spots were marked in red box in TEM image. (For interpretation of the references to colour in this figure legend, the reader is referred to the web version of this article.)

of abundant functional groups on the surfaces of the CDots. A broad peak spanning 3250–3700 cm<sup>−1</sup> indicated that the surfaces of the CDots were rich in —OH groups [14]. The peaks found at 1404 cm<sup>−1</sup> may also have been caused by the existence of —OH [14]. In addition, several peaks were observed at around 1245 cm<sup>−1</sup> (C—O—C), 1634 cm<sup>−1</sup> (C=O), 1718 cm<sup>−1</sup> and 1441 cm<sup>−1</sup> (C=C), and 1400 cm<sup>−1</sup> (C—O) [28]. The presence of the corresponding hydrophilic oxygen-containing groups was presumably conducive to the facile and homogeneous dispersion of the CDots in the aqueous solution, thus helping the CDots to combine uniformly with the main semiconductor [30]. In summary, the above results indicated that oxygen-containing functional groups were formed by electrochemical oxidation. In this process, a certain amount of the (*sp*<sup>2</sup>-hybridized) C=C bonds in graphite was decomposed into oxygen-containing functional groups in the CDots [28].

As shown in Fig. 2b, peaks appeared at 2900–3600 cm<sup>−1</sup> for both WO<sub>3</sub> indicating the O—H stretching vibrations of —OH group, and for CDots/WO<sub>3</sub> suggesting the C—H and O—H stretching vibrations of the COH group, respectively [29]. The set of peaks below 1100 cm<sup>−1</sup> can be ascribed to the O—W—O stretching modes of WO<sub>3</sub> [5]. The peaks at 3425 cm<sup>−1</sup> that appeared in both WO<sub>3</sub> nanorods and CDots/WO<sub>3</sub> were attributed to the vibrations of surface-adsorbed water [31]. In the FT-IR spectra of CDots/WO<sub>3</sub>, the absorption bands at 1635 cm<sup>−1</sup> were associated with the stretching vibrations of C=O, a consequence of the CDots [28,31]. It is worth noting that the peaks located at 1400 cm<sup>−1</sup> in the CDots, corresponding to the C—O stretching vibration, shifted to 1413 cm<sup>−1</sup> and were enhanced in intensity in the CDots/WO<sub>3</sub> nanocomposites [31]. We interpret this as further evidence of the strong interaction between CDots and WO<sub>3</sub> nanorods in the nanocomposites, as

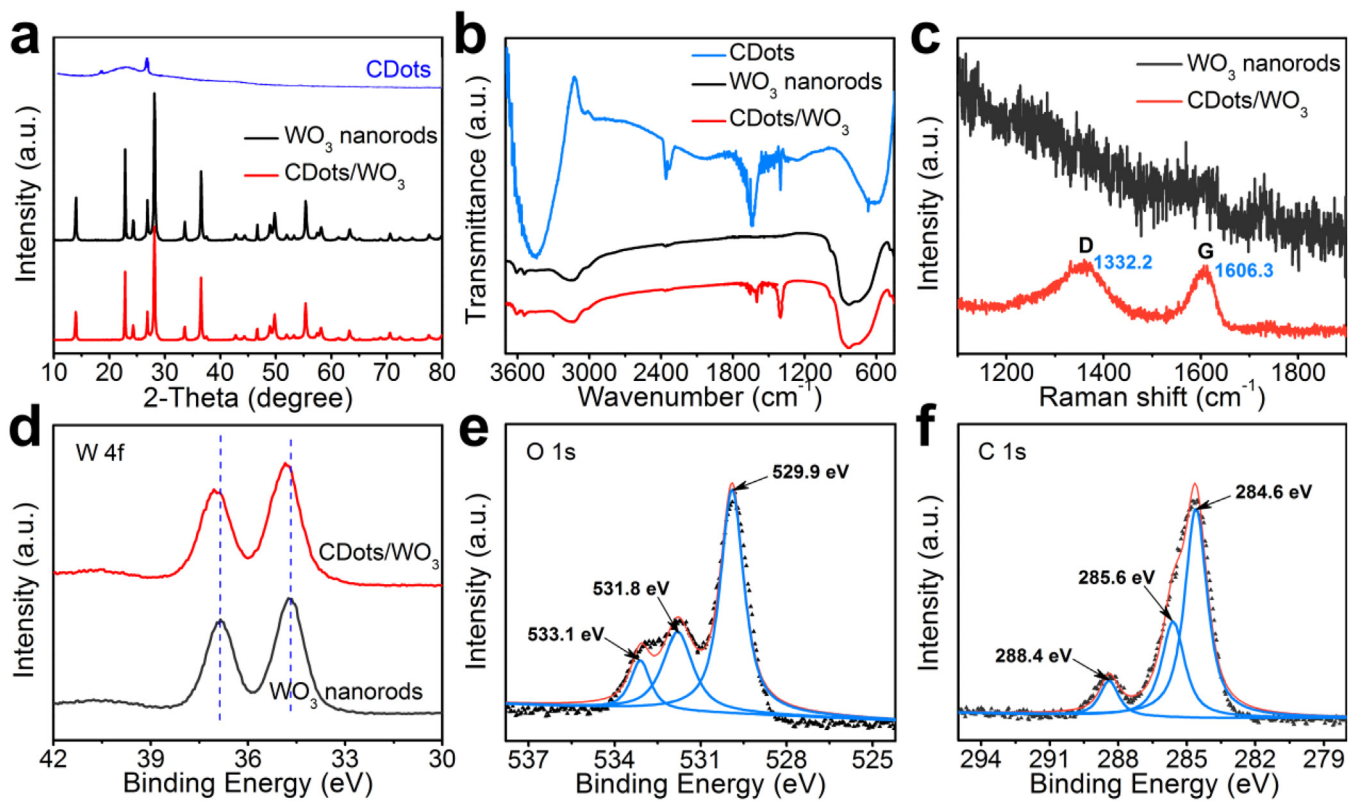


**Fig. 2.** The interaction between CDots and  $\text{WO}_3$  nanorods. a, Room temperature XRD patterns and b, FT-IR spectra of CDots,  $\text{WO}_3$  and CDots/ $\text{WO}_3$  nanocomposites, c, Raman spectra of  $\text{WO}_3$  and CDots/ $\text{WO}_3$  nanocomposites. XPS spectra for  $\text{WO}_3$  and CDots/ $\text{WO}_3$  nanocomposites, high-resolution XPS spectra of d, O 1s, e, W 4f and f, C 1s.

follows: after the CDots were deposited on the surface of the  $\text{WO}_3$  nanorods, new C–O bonds formed between them, with a different bond energy from the C–O bonds present in the isolated CDots [32]. This interaction thus caused a distinct peak shift.

The Raman spectra of the CDots/ $\text{WO}_3$  nanocomposites (Fig. 2c) contained two characteristic peaks that were not present in the spectra of the  $\text{WO}_3$  nanorods, located at about 1332.2 and 1606.3  $\text{cm}^{-1}$ , corresponding to the D-band and the G-band, respectively [8,15]. The D-band arose from the vibrations of carbon atoms in disordered graphite, while the G-band was attributed to an ordered graphite structure [15]. The intensity ratio of the D band to the G band ( $I_D/I_G$ ) is a measure of the ratio of  $\text{sp}^3/\text{sp}^2$  carbon in a sample, and shows the degree of graphitization of carbon. In the CDots/ $\text{WO}_3$ , this ratio was relatively high at 1.1. This indicated that the  $\text{WO}_3$  crystal structure of the CDots/ $\text{WO}_3$  nanocomposites contained a considerable amount of defects and lattice disorders corresponding to CDots, demonstrating the successful chemical combination of these two species [31].

The surface chemical composition of  $\text{WO}_3$  and CDots/ $\text{WO}_3$  samples, and the chemical interactions between CDots and  $\text{WO}_3$  were further confirmed by XPS analysis. The full XPS spectrum of CDots/ $\text{WO}_3$  (Fig. S5) confirmed the existence of O, W and C in the materials. For  $\text{WO}_3$  sample, the binding energies at 35.5, 37.5 and 41.7 eV corresponded to the spin-orbit splitting of the W 4f<sub>7/2</sub>, W 4f<sub>5/2</sub> and W 5p<sub>3/2</sub> components of tungsten oxides, respectively (Fig. 2d), suggesting that  $\text{W}^{6+}$  was the dominant valence state of W in the product [5]. The W 4f peak in the CDots/ $\text{WO}_3$  nanocomposites exhibited a slight shift when compared to those in the  $\text{WO}_3$  sample. This suggested that the surface chemical environment of W in the CDots/ $\text{WO}_3$  changed, which could be attributed to the presence of interaction between the CDots and  $\text{WO}_3$  [5,33]. The broad peak in the O 1s spectrum (Fig. 2e) could be resolved into three peaks centered at 529.9, 531.8 and 533.1 eV, which were identified

as the characteristic peaks of W–O, C=O and O–H bonds, respectively [5,29]. Fig. 2f displayed the XPS spectrum of the C 1s, which revealed the surface function groups on the CDots. Three peaks located at 284.6, 285.6 and 288.4 eV were attributed to C=O, C–C and  $\text{sp}^2$ -hybridized carbon, respectively [5,20].

From XRD, Raman, FT-IR and XPS analyses, it is obvious that the bonding between CDots and  $\text{WO}_3$  nanorods was efficiently formed, which was confirmed as the key to enhance the electronic separation and improve the photocatalytic activity by Wang et al. [1]. Taken together, these findings further confirmed the successful synthesis and the potential photocatalytic performance of the prepared CDots/ $\text{WO}_3$  nanocomposites.

The light-response characteristics of the as-prepared materials were investigated by UV-vis-NIR DRS, PL spectroscopy, photocurrent measurements and EIS measurements. Fig. 3a presents the evidently strong, broad and continuous spectrum-wide absorption by the prepared CDots in the UV, visible and especially NIR regions. Thus, the composite photocatalyst containing CDots could effectively utilize solar energy to photo-generate electron–hole pairs. The weak peak at around 300 nm was the characteristic absorption peak of polycyclic aromatic hydrocarbons ( $\pi$ – $\pi$  conjugated species), consistently with previous reports [29]. The DRS results thus provided further evidence that the CDots had formed from the aggregation of graphite fragments. The up-converted PL spectra (Fig. 3b) indicated that the CDots could be excited by long-wavelength light from 700 to 1000 nm, with the corresponding up-converted emissions located in the range from 345 to 575 nm, depending on the excitation wavelength. This excitation-dependent up-converted PL behavior of the CDots was probably attributable to the multiphoton active process, similar to that previously reported for carbon dots [13], which would enable the excited electrons to transfer to the acceptor (in contact with the sensitizer) either directly or indirectly.

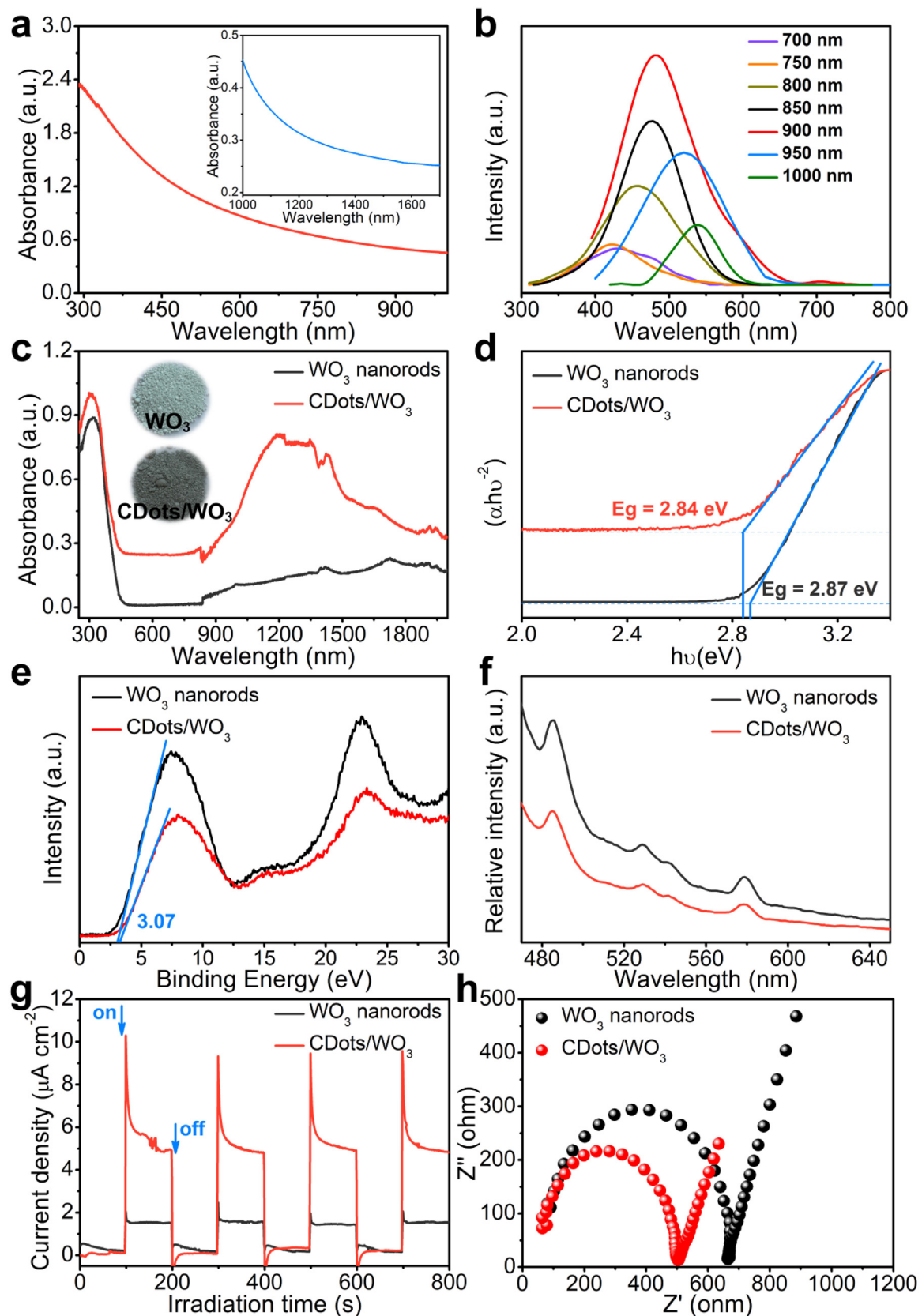


**Fig. 3.** Optical and charge migration properties of CDots,  $\text{WO}_3$  nanorods and CDots/ $\text{WO}_3$  nanocomposites. a, UV-vis–NIR absorption spectrum of CDots. b, Up-converted PL spectra of CDots with different excitation wavelengths from 700 to 1000 nm with the interval of 50 nm. c, UV-vis–NIR DRS with insets for the colors of prepared samples; d, Band gap values, estimated from the plotted curve of  $(\alpha h\nu)^{1/2}$  vs  $h\nu$ ; e, XPS valence band spectrum; f, PL spectra; g, Transient photo-current response and h, Electrochemical impedance spectroscopy.

**Fig. 3c** compares the UV–vis–NIR DRS spectra of  $\text{WO}_3$  and CDots/ $\text{WO}_3$ , in which the prepared CDots/ $\text{WO}_3$  showed much greater light absorption across the entire examined spectral region. The  $\text{WO}_3$  nanorods only appreciably absorbed visible light with wavelengths shorter than 475 nm, in agreement with a previous report [24]. In contrast, the CDots/ $\text{WO}_3$  showed intense and wide absorption across the UV–vis region, implying the production of more photo-generated electron–hole pairs and a higher photocatalytic activity under this wavelength of irradiation. Unlike the  $\text{WO}_3$  nanorods, the CDots/ $\text{WO}_3$  showed continuous strong absorption in the NIR region (780–2000 nm), which is conducive to the full-spectrum utilization of solar light. The CDots evidently played an important role in enhancing the light-absorption capacity of the CDots/ $\text{WO}_3$ , as the absorption intensity increased with the increment in the amount of CDots (Fig. S6).

As shown in **Fig. 3d**, the optical band gaps ( $E_g$ ) of the  $\text{WO}_3$  nanorods and CDots/ $\text{WO}_3$  were calculated as the slopes of the curves of converted  $(\alpha h\nu)^r$  versus  $h\nu$ , where  $\alpha$ ,  $h$  and  $\nu$  are the absorption coefficient, Planck constant and light frequency, respectively, and  $r=1/2$  for an indirect-band-gap material and  $r=2$  for a direct-band-gap material [34]. In our case, good linear fits were obtained when using  $r=2$ , in agreement with previous reports describing  $\text{WO}_3$  as a direct-band-gap material. The resulting calculated  $E_g$  values of the  $\text{WO}_3$  nanorods and CDots/ $\text{WO}_3$  were 2.87 and 2.84 eV (represented by the black and red curves in **Fig. 3d**), respectively. The similar  $E_g$  values indicated that the optical band gap of the  $\text{WO}_3$  nanorods remained almost completely unchanged after the addition of CDots. In addition, the DRS spectrum of the CDots/ $\text{WO}_3$  displayed an obvious tail between 2.3 and 2.8 eV, implying an enhanced photo-response and photocatalytic efficiency. Furthermore, we used the XPS valence band spectra of the  $\text{WO}_3$  nanorods and CDots/ $\text{WO}_3$  to determine their VB gaps ( $E_v$ ), and both were calculated to be approximately 3.07 eV (**Fig. 3e**). This allowed the CB gaps ( $E_c$ ) of the  $\text{WO}_3$  nanorods and CDots/ $\text{WO}_3$  to be estimated at 0.23 and 0.20 eV, respectively, from  $E_c = E_v - E_g$ . According to Wang et al. [1], a relatively high CB gap is favorable for heterostructure formation and charge-carrier transport. In addition to an appropriate band gap, the proper matching of the CB and VB levels of a photocatalyst with the redox potentials of the desired photocatalytic reactions is also important for photocatalytic degradation [1,7].

**Fig. 3f** presents the PL spectra of the  $\text{WO}_3$  and CDots/ $\text{WO}_3$ . Both exhibited an emission peak centered at around 480 nm under excitation at 325 nm, in good agreement with the position of the absorption edge in the UV–vis–NIR DRS spectra (**Fig. 3c**). The intensity of the emission peak for the CDots/ $\text{WO}_3$  decreased significantly compared with that for the  $\text{WO}_3$  nanorods, indicating that the CDots on the surface of the  $\text{WO}_3$  nanorods facilitated electron transfer and inhibited the recombination of the photo-generated charge carriers [5,25].

It was also confirmed by the photo-current and EIS measurements (**Fig. 3g** and **h**) that the introduction of CDots reduced the electron–hole recombination rate. The photo-current responses of both electrodes changed considerably once the light was switched on/off, with steady and reproducible results during several consecutive on–off irradiation cycles (**Fig. 3g**). The photo-current intensity of the CDots/ $\text{WO}_3$  was ~2.9 times higher than that of the  $\text{WO}_3$  nanorods, suggesting a higher separation rate of photo-excited electrons and holes in the CDots/ $\text{WO}_3$  nanocomposites under visible-light irradiation [27]. A possible mechanism of this separation was that, after the photo-generated electrons were excited from the VB to the CB of  $\text{WO}_3$ , they were then transferred to the CDots, inhibiting the direct recombination of electrons and holes. The CDots were likely to have been good electron acceptors because of their conjugated  $\pi$  structure, making them efficient separation centers of the photo-excited charge carriers [30]. EIS measurements

of the  $\text{WO}_3$  nanorods and CDots/ $\text{WO}_3$  nanocomposites were carried out to investigate the process of electron transfer (**Fig. 3h**). The arc radius of the EIS Nyquist plot of the CDots/ $\text{WO}_3$  was much smaller than that of the  $\text{WO}_3$  nanorods, implying a faster rate of interfacial charge transfer to the electron acceptors in the former, resulting in the effective separation of electron–hole pairs [5,8].

### 3.2. Photocatalytic performance

As shown in **Fig. 4a–c**, the concentration of RhB showed no appreciable change under UV, visible or NIR irradiation, indicating that the RhB was photo-chemically stable. The prepared  $\text{WO}_3$  nanorods and CDots/ $\text{WO}_3$  achieved ~20% and 25% removal efficiency of RhB by adsorption, respectively, with no apparent adsorption over pure CDots or commercial  $\text{WO}_3$  nanoparticles (**Fig. 4a–c**).

Whether under UV, visible-light or NIR irradiation, the removal efficiencies of RhB always decreased in the order CDots/ $\text{WO}_3$  > prepared  $\text{WO}_3$  nanorods > commercial  $\text{WO}_3$  nanoparticles. For instance, under visible light, the CDots/ $\text{WO}_3$  nanocomposites exhibited an RhB removal efficiency of 99.1% in 140 min, while the corresponding efficiencies of the  $\text{WO}_3$  nanorods and commercial  $\text{WO}_3$  were 69.1% and 11.6%, respectively, under the same condition. The CDots/ $\text{WO}_3$  showed higher photocatalytic activity than the  $\text{WO}_3$  nanorods under both UV and visible-light irradiation, mainly because of the stronger light absorption and the more efficient electron-transfer capability of the CDots/ $\text{WO}_3$  (**Fig. 3**). Moreover, the CDots/ $\text{WO}_3$  presented significant capability for photocatalytic RhB degradation (61.2% in 480 min) under light wavelengths longer than 780 nm (NIR light), while neither the  $\text{WO}_3$  nanorods nor commercial  $\text{WO}_3$  achieved any noticeable degradation. These results demonstrated that the introduction of CDots significantly improved the photocatalytic activity of the  $\text{WO}_3$  nanorods under a broad spectrum of light including UV, Vis and NIR frequencies. By contrast, in  $\text{WO}_3$  nanorods, only light with wavelengths shorter than 475 nm could be used to photo-generate electron–hole pairs; therefore, the up-converted PL behavior of the CDots effectively extended the photo-active wavelengths of the CDots/ $\text{WO}_3$  to the NIR region. To quantitatively understand the degradation of RhB, the degradation kinetics was investigated by fitting the experimental data to the Langmuir–Hinshelwood model under UV, visible and NIR irradiation (Fig. S8 and Table S2) [35]. The CDots/ $\text{WO}_3$  possessed a higher apparent reaction rate constant ( $k$  value) than those of the prepared  $\text{WO}_3$  nanorods and commercial  $\text{WO}_3$  nanoparticles, indicating higher activity under UV, visible and NIR irradiation. In addition, the mineralization efficiency of RhB were ~88.1%, 89.8% and 45.3% for CDots/ $\text{WO}_3$  under UV, visible and NIR light irradiation, which were much higher than other materials under the identical conditions (Fig. S9).

To eliminate the effect of dye photo-sensitization and further evaluate the application potential of CDots/ $\text{WO}_3$ , tests were performed using TCH and phenol as the target pollutants. The prepared  $\text{WO}_3$  nanorods exhibited a TCH removal efficiency of only 40.8% in 3.5 h under visible-light irradiation, while the CDots/ $\text{WO}_3$  achieved a roughly 2-fold higher efficiency (78.6%) under the same conditions (**Fig. 4d**). The fitting of the TCH degradation to the Langmuir–Hinshelwood model is shown in Table S2 and Fig. S10. The calculated  $k$  value for the CDots/ $\text{WO}_3$  nanocomposites was  $0.403 \text{ h}^{-1}$ , which was 2.9 times higher than that of the  $\text{WO}_3$  nanorods ( $0.139 \text{ h}^{-1}$ ). The phenol removal efficiencies were ~70.2% and 34.7% for the CDots/ $\text{WO}_3$  and  $\text{WO}_3$  nanorods, respectively, under visible-light irradiation in 4 h (**Fig. 4e**). The calculated  $k$  values showed similar trends (Fig. S10 and Table S2). Also, **Fig. 4f** shows that the mineralization efficiency of phenol by the CDots/ $\text{WO}_3$  was 55.9%, much higher than that by the  $\text{WO}_3$  nanorods (20%). These results clearly demonstrated that the photocatalytic activity of the

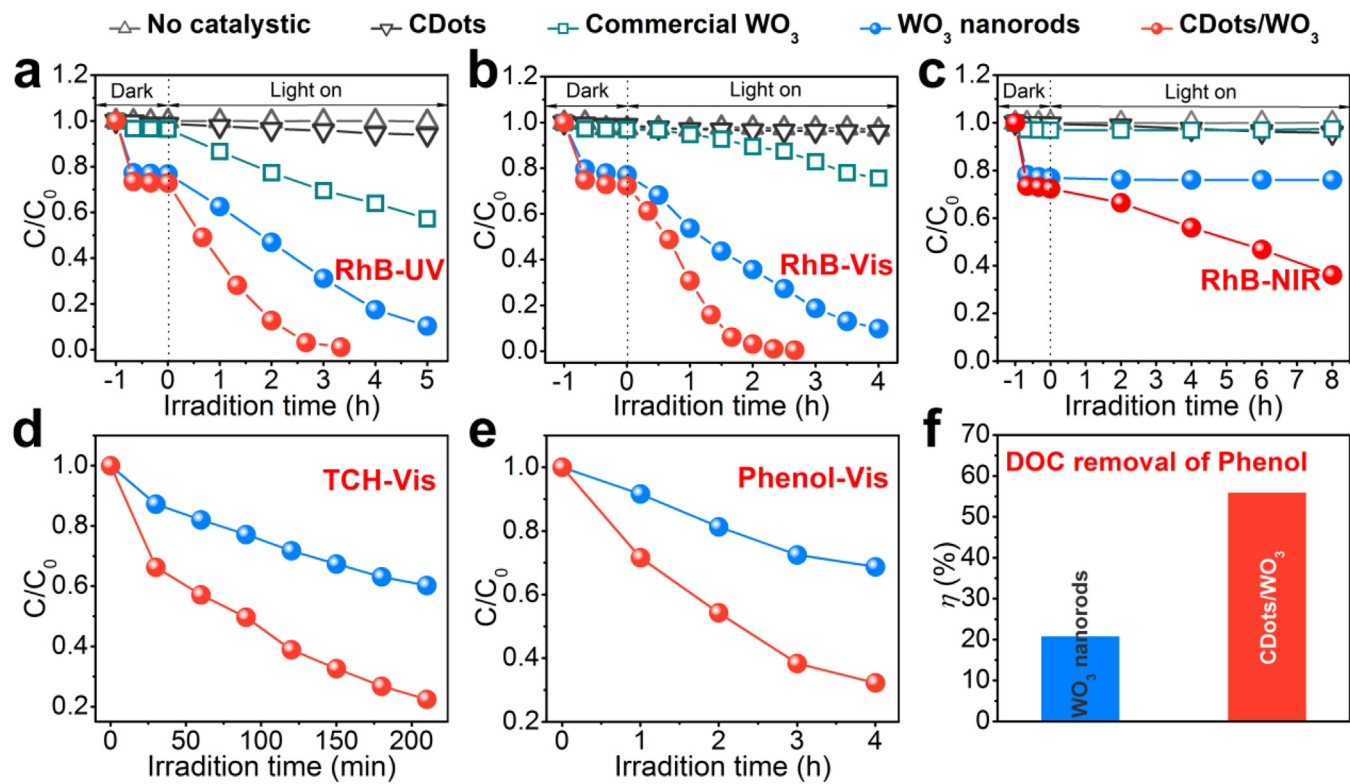


**Fig. 4.** Photocatalytic degradation of RhB by prepared  $\text{WO}_3$  and CDots/ $\text{WO}_3$  under a, UV, b, visible, and c, NIR light irradiation; and d, e and f Photocatalytic degradation of TCH, phenol and DOC removal efficiency of phenol under visible light irradiation. Photocatalytic degradation conditions: 100 mL solution (10 mg  $\text{L}^{-1}$  RhB, 20 mg  $\text{L}^{-1}$  TCH and 20 mg  $\text{L}^{-1}$  phenol), light source (150 W xenon lamp with different emission region by various filters as presented in Fig. S1), pH (neutral), temperature (ca. 20 °C), magnetic stirring rate (500 rpm).

$\text{WO}_3$  nanorods was markedly improved after the deposition of CDots, and that the CDots played an important role in the activity of the CDots/ $\text{WO}_3$  nanocomposites.

### 3.3. Photocatalytic mechanism

To investigate the photocatalytic mechanism of the CDots/ $\text{WO}_3$  nanocomposites, scavenger-quenching experiments were performed to compare the photocatalytic capabilities of each of the reactive oxidation species (ROSs) potentially involved in the reaction. The proposed ROSs, namely,  $\text{e}^-$ ,  $\text{O}_2^-$ ,  $\cdot\text{OH}$  and  $\text{h}^+$ , were quenched using four different scavengers:  $\text{Cr}^{6+}$ , TEMPO, isopropanol and sodium oxalate, respectively. First of all, it was worth noting that the reaction time for  $\text{WO}_3$  and CDots/ $\text{WO}_3$  were 260 and 160 min, respectively. As shown in Fig. 5,  $\text{e}^-$  and  $\text{h}^+$  were the main ROSs present in the  $\text{WO}_3$  nanorods system, while  $\text{O}_2^-$  and  $\cdot\text{OH}$  were scarce. In contrast, all four types of ROS were present in the CDots/ $\text{WO}_3$  nanocomposite system, which was consistent with the faster photocatalytic rate of this system compared with the  $\text{WO}_3$  nanorods (Fig. 5). In the CDots/ $\text{WO}_3$  system, the effect of the scavengers on the reaction rate decreased in the order sodium oxalate (for  $\text{h}^+$ ) > TEMPO (for  $\text{O}_2^-$ ) > isopropanol (for  $\cdot\text{OH}$ ) >  $\text{Cr}^{6+}$  (for  $\text{e}^-$ ). Comparing the  $\text{WO}_3$  nanorods with the CDots/ $\text{WO}_3$ ,  $\text{h}^+$  was an important ROS in both systems, while the  $\text{e}^-$  concentration was sharply reduced in CDots/ $\text{WO}_3$ . However, the emergence of  $\text{O}_2^-$  and  $\cdot\text{OH}$  in the latter indicated that they played a critical role and made a large contribution to the photo-degradation of RhB. The emergence of both these ROSs in CDots/ $\text{WO}_3$  may have been a consequence of the fast electron transfer rate. The additional photo-generated electrons may have combined with the adsorbed  $\text{O}_2$  to form  $\text{O}_2^-$ , thus greatly enhancing the photocatalytic performance. Moreover, the fast electron transfer rate may have promoted the

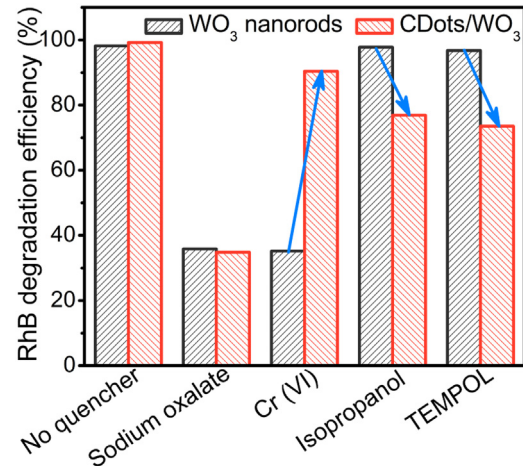


**Fig. 5.** Quenching experiment of active-species during the photocatalytic degradation of RhB over  $\text{WO}_3$  nanorods and CDots/ $\text{WO}_3$  under visible light irradiation. Photocatalytic degradation conditions: (100 mL solution of 10 mg  $\text{L}^{-1}$  RhB), light source (filtered 150 W xenon lamp with visible light emission only), pH (neutral), temperature (ca. 20 °C), magnetic stirring rate (500 rpm) and reaction time (160 min for CDots/ $\text{WO}_3$  and 260 min for  $\text{WO}_3$  nanorods).

generation of  $\cdot\text{OH}$  from both  $\text{h}^+$  and  $\text{O}_2^-$ , thus further enhancing the photo-degradation rate. It was worth mentioning that almost no  $\text{O}_2^-$  and  $\cdot\text{OH}$  were present in the  $\text{WO}_3$  nanorods system, indicating that the  $\text{WO}_3$  nanorods were unable to generate those ROSs under visible-light irradiation. However, after the introduction of CDots, both  $\text{O}_2^-$  and  $\cdot\text{OH}$  appeared in the CDots/ $\text{WO}_3$  system, having most likely been produced on the surface of the CDots.

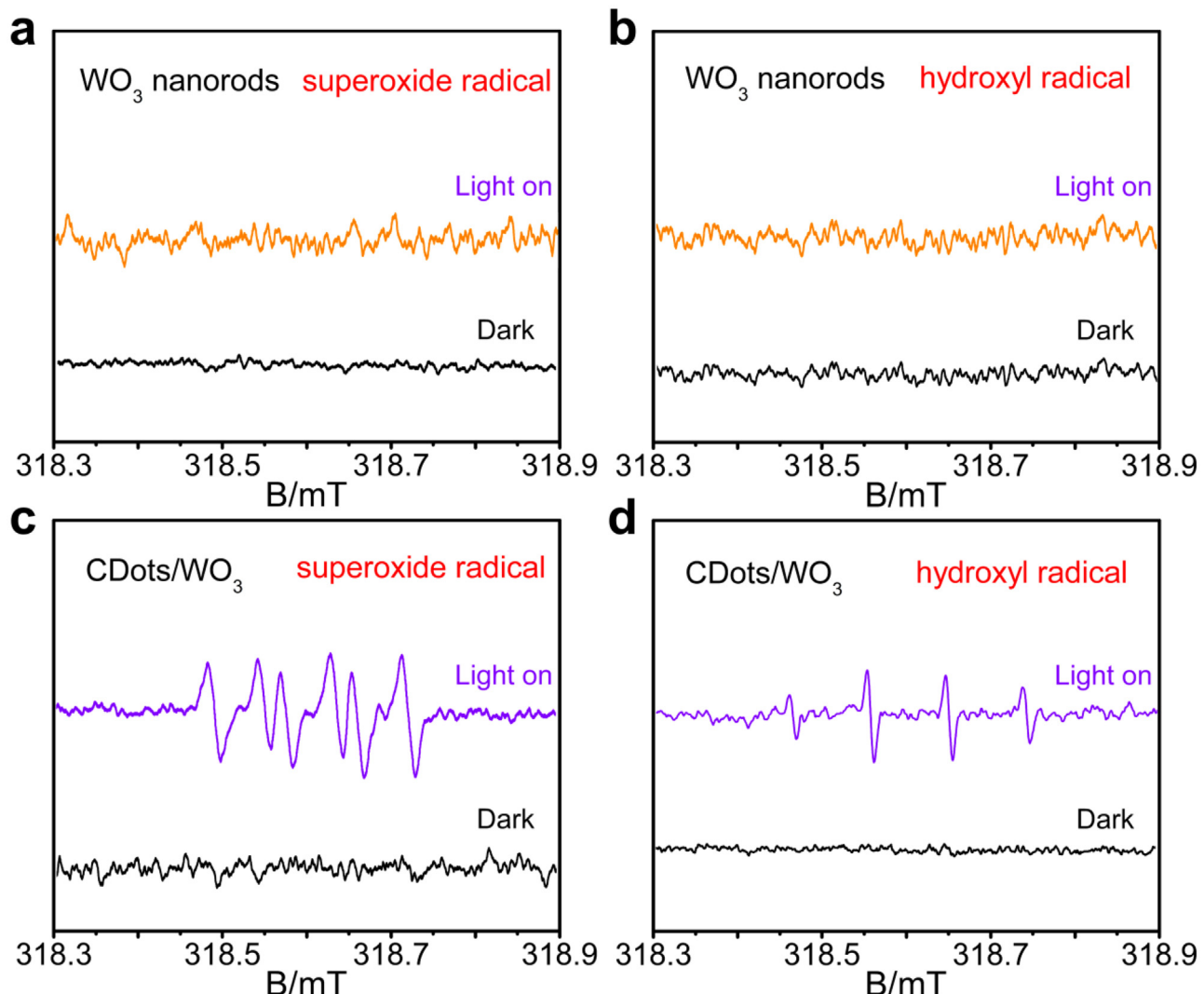
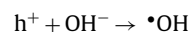


**Fig. 6.** DMPO spin-trapping ESR spectra recorded with (a and b)  $\text{WO}_3$  nanorods and (c and d) CDots/ $\text{WO}_3$  nanocomposites under visible light irradiation. The dispersion solutions were methanol and water for the detection of DMPO- $\cdot\text{O}_2^-$  and DMPO- $\cdot\text{OH}$ , respectively).

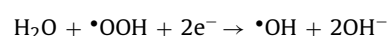
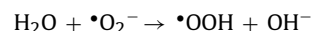
To further confirm the active species and reveal the photodegradation mechanism on the photoreaction process, the ESR spin-trap technique was then performed for  $\text{WO}_3$  nanorods and CDots/ $\text{WO}_3$  nanocomposites with DMPO in methanol and  $\text{H}_2\text{O}$ . DMPO is a nitroxyl spin trap generally used for trapping radicals due to the generation of stable free radicals, DMPO- $\cdot\text{O}_2^-$  or DMPO- $\cdot\text{OH}$  [33]. As shown in Fig. 6a and b, negligible signals of DMPO- $\cdot\text{O}_2^-$  and DMPO- $\cdot\text{OH}$  were found for  $\text{WO}_3$ , revealing that  $\cdot\text{O}_2^-$  and  $\cdot\text{OH}$  may be not the main active species under visible light irradiation. It was consistent with the results of scavenger-quenching experiments (see Fig. 5). In contrast, after the modification of CDots on the  $\text{WO}_3$ , both the signal of DMPO- $\cdot\text{O}_2^-$  and DMPO- $\cdot\text{OH}$  can be found clearly (Fig. 6c and d). It indicated that the  $\cdot\text{O}_2^-$  and  $\cdot\text{OH}$  were produced in the CDots/ $\text{WO}_3$  system, which contributed to the higher photocatalytic activity of CDots/ $\text{WO}_3$  materials [33].

The standard redox potential of  $\text{O}_2/\cdot\text{O}_2^-$  has been established as  $-0.33\text{ V}$  (vs. NHE). Thus, in order to generate  $\cdot\text{O}_2^-$  on the surface of a semiconductor photocatalyst, the CB position should be more negative than this value. However, the CB of the prepared  $\text{WO}_3$  nanorods was positioned at about  $0.23\text{ eV}$ , far more positive than the reduction potential of  $\text{O}_2/\cdot\text{O}_2^-$ . Thus, the photo-generated electrons ( $e^-$ ) on the surface of the  $\text{WO}_3$  nanorods were thermodynamically unable to react with  $\text{O}_2$  to produce  $\cdot\text{O}_2^-$ . The  $\cdot\text{O}_2^-$

would appear only if the CB potential was satisfied with the thermodynamic potentials of  $\text{O}_2/\cdot\text{O}_2^-$ . In contrast, a significant amount of  $\cdot\text{O}_2^-$  appeared in the CDots/ $\text{WO}_3$  nanocomposite system, suggesting that the CDots acted as a co-catalyst, with an appropriate CB position to produce  $\cdot\text{O}_2^-$ . Indeed, previous studies have confirmed that the CB in CDots is positioned at around  $-1.16\text{ eV}$  [25]. Therefore, the  $e^-$  generated in the CB of the CDots could react with  $\text{O}_2$  to produce  $\cdot\text{O}_2^-$ . This was consistent with the results of the scavenger-quenching experiments and ESR analysis (Figs. 5 and 6). Similarly, the VB position of the  $\text{WO}_3$  nanorods was  $+3.07\text{ eV}$ , which was more positive than the standard redox potential of  $\cdot\text{OH}/\text{OH}^-$  ( $2.3\text{ eV}$  vs. NHE). In theory,  $\cdot\text{OH}$  could have formed on the surface of the  $\text{WO}_3$  nanorods through the following reaction:



However, almost no  $\cdot\text{OH}$  was present in the  $\text{WO}_3$  nanorods system. In contrast,  $\cdot\text{OH}$  was detected when the CDots/ $\text{WO}_3$  was used as the catalyst. The  $\cdot\text{OH}$  that appeared in the CDots/ $\text{WO}_3$  system was therefore produced by the following reactions:



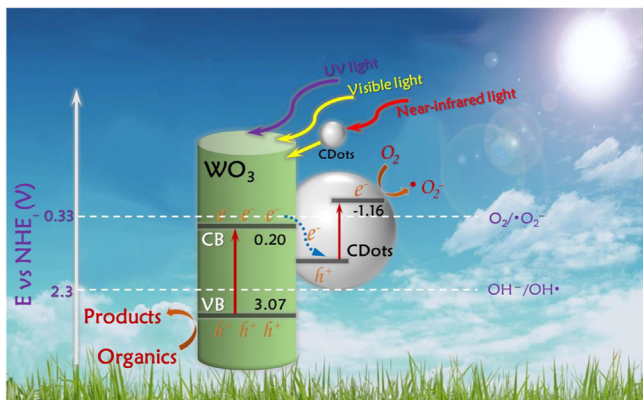
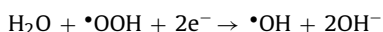
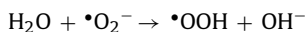
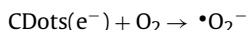
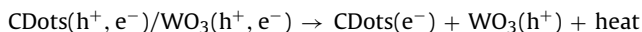
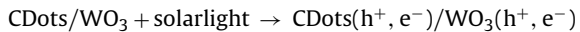


**Fig. 7.** Schematic photocatalytic mechanism for the CDots/WO<sub>3</sub> nanocomposites under UV, visible and NIR light irradiation.

On the basis of the above results, a charge-transfer mechanism for the CDots/WO<sub>3</sub> nanocomposite was proposed, as shown in Fig. 7. In the CDots/WO<sub>3</sub> heterostructure, part of the surface of the WO<sub>3</sub> nanorods was covered by CDots, constituting a CDots/WO<sub>3</sub> Z-scheme photocatalytic system. Under solar irradiation, both WO<sub>3</sub> and CDots were photo-excited, generating e<sup>-</sup>/h<sup>+</sup> pairs. The h<sup>+</sup> generated in WO<sub>3</sub> remained in the VB of WO<sub>3</sub>. However, the e<sup>-</sup> in the CB of WO<sub>3</sub> transferred to the VB of the CDots, and combined with the h<sup>+</sup> in the VB of the CDots through the contact interface between CDots and WO<sub>3</sub> nanorods. Accordingly, the efficient spatial separation of the photo-generated e<sup>-</sup>/h<sup>+</sup> pairs was realized. Subsequently, the h<sup>+</sup> stored in the VB of WO<sub>3</sub> migrated to the surface of WO<sub>3</sub> and directly decomposed the surface-adsorbed organics, while the enriched e<sup>-</sup> content in the CB of the CDots likely favored the generation of •O<sub>2</sub><sup>-</sup> (which also promoted degradation of the organics) because of the reduced electron–hole recombination. Thus, the oxidation and reduction of the organic pollutants occurred separately on the surfaces of the two different materials. Based on the discussion above, the major reactions in this system would have been as follows:



No electron mediator was present between the WO<sub>3</sub> nanorods and CDots; rather, the photo-generated e<sup>-</sup> transferred directly through the interfacial contact. This Z-scheme heterostructure not only promoted the separation of photo-generated e<sup>-</sup>/h<sup>+</sup> pairs but also improved the redox ability of the photocatalyst because of the enhanced redox potential. The formation of a Z-scheme heterostructure effectively extended the lifetime of the photo-generated charge carriers, thus promoting the redox ability of the system [27,36].

In contrast, if WO<sub>3</sub> and CDots had formed a conventional CDots/WO<sub>3</sub> heterostructure (Type-II), the photo-generated e<sup>-</sup> would have transferred from the CB of the CDots to the CB of the WO<sub>3</sub> nanorods spontaneously. The h<sup>+</sup> in the VB of the WO<sub>3</sub> nanorods would have transferred to the VB of CDots to form a Type-II heterostructure. Although the spatial separation of the photo-generated e<sup>-</sup>/h<sup>+</sup> pairs would still have been achieved, it would have weakened the redox potential of photocatalysis [36]. In

this case, the e<sup>-</sup> gathered on the surface of the WO<sub>3</sub> nanorods would have been unable to combine with O<sub>2</sub> to generate •O<sub>2</sub><sup>-</sup> because of the lower CB potential of the system. As a result, no •O<sub>2</sub><sup>-</sup> would have been detected in a Type-II CDots/WO<sub>3</sub> system, in contradiction to the experimental finding (see in Figs. 5 and 6). Therefore, it can be concluded that the WO<sub>3</sub> nanorods and CDots did not form a Type-II heterostructure. Instead, the mechanistic evidence indicates that a direct Z-scheme photocatalytic system was formed in the CDots/WO<sub>3</sub>.

In the above discussion, we have proposed a complete photocatalytic mechanism for the CDots/WO<sub>3</sub> nanocomposites under UV, visible and NIR irradiation (Fig. 7). Three main processes occurred in the CDots/WO<sub>3</sub> nanocomposites under solar irradiation. (1) Both WO<sub>3</sub> nanorods and CDots could be excited by UV and short-wavelength visible light, thus photo-generating e<sup>-</sup>/h<sup>+</sup> pairs. Moreover, the CDots could also efficiently absorb longer-wavelength visible and NIR light, which was then transformed by up-conversion into shorter-wavelength light, which in turn was absorbed by the WO<sub>3</sub> nanorods to produce additional photo-generated e<sup>-</sup>/h<sup>+</sup> pairs. Hence, the entire spectrum of solar light energy could be utilized efficiently. (2) A direct Z-scheme heterostructure was formed after the CDots were introduced to the surface of the WO<sub>3</sub> nanorods. This contact interface resulted in the recombination of the photo-generated e<sup>-</sup> in WO<sub>3</sub> with the h<sup>+</sup> in the CDots, preventing the recombination of e<sup>-</sup>/h<sup>+</sup> pairs from WO<sub>3</sub>. Therefore, a greater amount of e<sup>-</sup> with a relatively low CB potential, as well as h<sup>+</sup> with a relatively high VB potential, could be retained, which contributed to the enhanced photocatalytic ability. Furthermore, the spatial separation of e<sup>-</sup>/h<sup>+</sup> pairs ensured that the oxidation and reduction reactions occurred in two different regions. (3) The organic pollutants in the solution were efficiently adsorbed by the large number of active sites in CDots/WO<sub>3</sub>. In turn, the organics were effectively oxidized and hence removed by the generated ROSs, including e<sup>-</sup>, h<sup>+</sup>, •OH and •O<sub>2</sub><sup>-</sup>. The pollutants were degraded to intermediate products or even to H<sub>2</sub>O and CO<sub>2</sub> after the processes of aromatic-ring opening.

### 3.4. Recycling reactions

Two of the most important parameters for the practical application of a photocatalyst are its stability and reusability. Cycling tests of RhB photo-degradation were thus performed under UV, visible and NIR irradiation. As depicted in Fig. 8a, the activity of the CDots/WO<sub>3</sub> nanocomposites remained almost unchanged after 5 cycles under identical experimental conditions, i.e., the RhB removal efficiencies varied from 99.7% to 97.1% under UV light in 200 min, 99.6% to 97.7% under visible light in 160 min and 62.7% to 60.1% under NIR light in 480 min. This demonstrated that the prepared photocatalyst was stable, even with long reaction durations. Moreover, both the CDots/WO<sub>3</sub> and WO<sub>3</sub> nanorods exhibited high stability and reusability (Figs. 8 a and S11), with only slight decreases of the degradation efficiency after 5 cycles. The physical structure and optical-absorption ability of the fresh and recycled CDots/WO<sub>3</sub> samples were also carefully compared by XRD, XPS and DRS analysis (Fig. 8b–d). There were no significant differences between the fresh and recycled samples, indicating the excellent robustness of the CDots/WO<sub>3</sub> nanojunction. The above results confirmed that the CDots/WO<sub>3</sub> nanocomposites were stable after repeated recycling.

## 4. Conclusion

In this paper, we successfully synthesized a direct Z-scheme CDots/WO<sub>3</sub> nanocomposite via a facile process for the first time. The as-prepared CDots/WO<sub>3</sub> exhibited strongly enhanced photo-

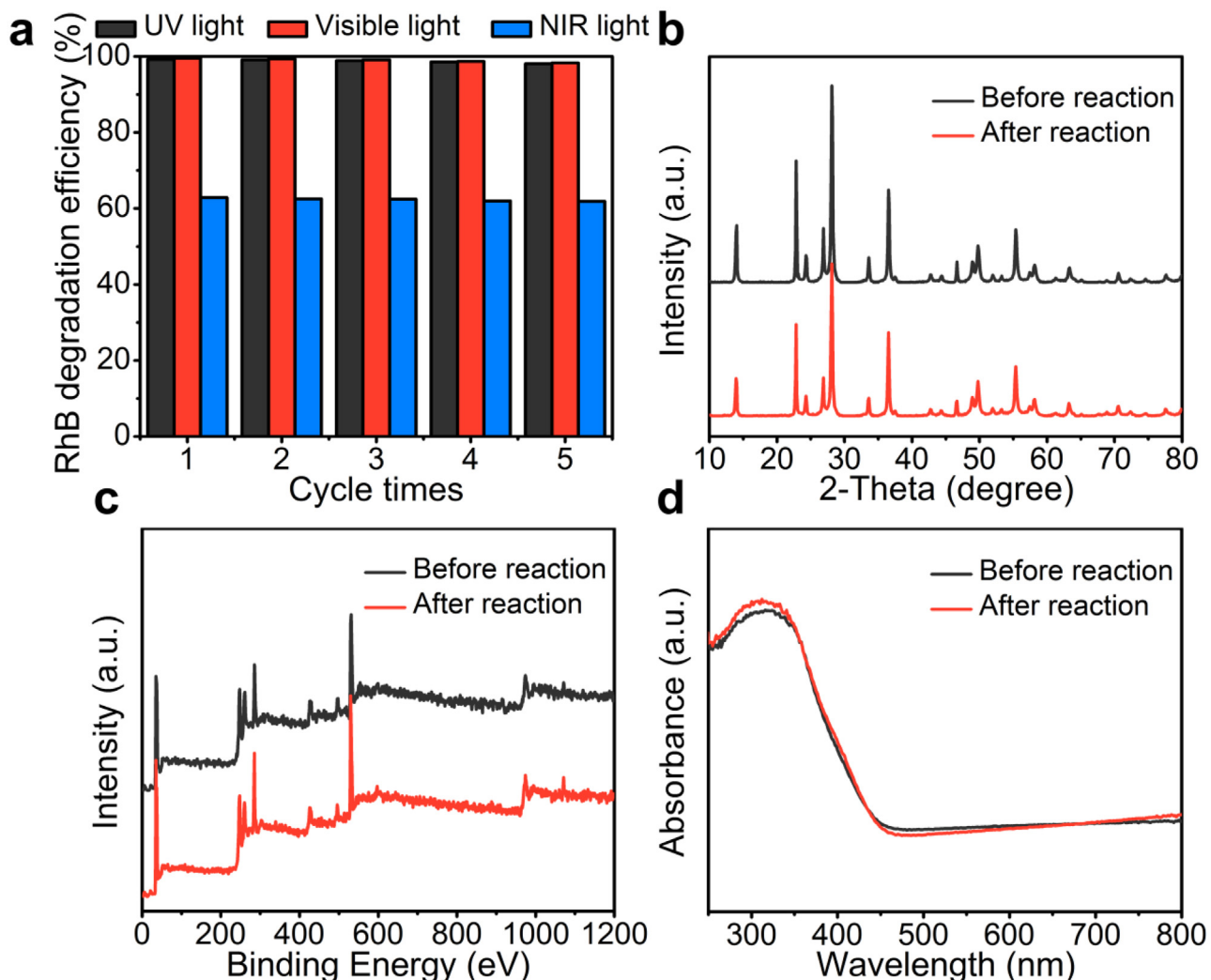


**Fig. 8.** Stability and reusability of CDots/WO<sub>3</sub> nanocomposites. a, Recycling runs of photocatalytic activity of the CDots/WO<sub>3</sub> nanocomposites toward RhB photo-degradation under UV, visible and NIR light irradiation. Physical characterizations of the CDots/WO<sub>3</sub> nanocomposites before and after the repeated photocatalytic degradation experiments in visible irradiation. b, XRD pattern; c, Full XPS spectra; d, UV-vis DRS spectra. Photocatalytic degradation conditions: 100 mL solution of 10 mg L<sup>-1</sup> RhB, light source (150 W xenon lamp with different emission region by various filters as presented in Fig. S1), pH (neutral), temperature (ca. 20 °C), magnetic stirring rate (500 rpm).

catalytic performance for the photo-degradation of RhB, TCH and phenol, and also showed increased mineralization efficiency, compared with the prepared WO<sub>3</sub> nanorods and commercial WO<sub>3</sub> nanoparticles under UV, Vis or NIR irradiation. On the basis of TEM, SEM, XPS, UV-vis-NIR DRS and PL analyses, scavenger-quenching experiments and ESR analysis, a possible mechanism was proposed for the photocatalytic reaction process. Two potential factors causing the improved performance of the system were identified, namely, its enhanced photo-response and effective spatial separation of photo-generated e<sup>-</sup>/h<sup>+</sup> pairs. In summary, this work demonstrated that an all-solid-state direct Z-scheme CDots/WO<sub>3</sub> nanocomposite could be accurately prepared, and displayed an excellent photocatalytic performance, representing a crucial advance in the synthesis of Z-scheme photocatalytic systems.

## Acknowledgements

This work was financially supported by the National Natural Science Foundation of China(51678270), the State Key Laboratory of Urban Water Resource and Environment, Harbin Institute of Tech-

nology (QA201418) and the Science and Technology Development Program of Jilin province, China (20140101159JC) financial.

## Appendix A. Supplementary data

Supplementary data associated with this article can be found, in the online version, at <http://dx.doi.org/10.1016/j.apcatb.2017.03.017>.

## References

- [1] H.L. Wang, L.S. Zhang, Z.G. Chen, J.Q. Hu, S.J. Li, Z.H. Wang, J.S. Liu, X.C. Wang, Chem. Soc. Rev. 43 (2014) 5234–5244.
- [2] X.X. Chen, Y.P. Li, X.Y. Pan, D. Cortie, X.T. Huang, Z.G. Yi, Nat. Commun. 7 (2016).
- [3] Y. Zheng, L.H. Lin, B. Wang, X.C. Wang, Angew. Chem. Int. Ed. 54 (2015) 12868–12884.
- [4] Q. Li, X. Li, S. Wageh, A.A. Al-Ghamdi, J.G. Yu, Adv. Energy Mater. 5 (2015).
- [5] J. Di, J.X. Xia, Y.P. Ge, H.P. Li, H.Y. Ji, H. Xu, Q. Zhang, H.M. Li, M.N. Li, Appl. Catal. B-Environ. 168 (2015) 51–61.
- [6] N. Wei, H.Z. Cui, Q. Song, L.Q. Zhang, X.J. Song, K. Wang, Y.F. Zhang, J. Li, J. Wen, J. Tian, Appl. Catal. B-Environ. 198 (2016) 83–90.
- [7] X. Li, J.G. Yu, M. Jaroniec, Chem. Soc. Rev. 45 (2016) 2603–2636.
- [8] J.G. Hou, H.J. Cheng, C. Yang, O. Takeda, H.M. Zhu, Nano Energy 18 (2015) 143–153.

- [9] J. Di, J.X. Xia, M.X. Ji, L. Xu, S. Yin, Q. Zhang, Z.G. Chen, H.M. Li, *Carbon* 98 (2016) 613–623.
- [10] B.C.M. Martindale, G.A.M. Hutton, C.A. Caputo, E. Reissner, *J. Am. Chem. Soc.* 137 (2015) 6018–6025.
- [11] G.L. Li, C.S. Guo, M. Yan, S.Q. Liu, *Appl. Catal. B-Environ.* 183 (2016) 142–148.
- [12] J. Liu, Y. Liu, N.Y. Liu, Y.Z. Han, X. Zhang, H. Huang, Y. Lifshitz, S.T. Lee, J. Zhong, Z.H. Kang, *Science* 347 (2015) 970–974.
- [13] H.T. Li, X.D. He, Z.H. Kang, H. Huang, Y. Liu, J.L. Liu, S.Y. Lian, C.H.A. Tsang, X.B. Yang, S.T. Lee, *Angew. Chem. Int. Ed.* 49 (2010) 4430–4434.
- [14] X. Zhang, F. Wang, H. Huang, H.T. Li, X. Han, Y. Liu, Z.H. Kang, *Nanoscale* 5 (2013) 2274–2278.
- [15] H.C. Zhang, H. Huang, H. Ming, H.T. Li, L.L. Zhang, Y. Liu, Z.H. Kang, *J. Mater. Chem.* 22 (2012) 10501–10506.
- [16] J.X. Xia, J. Di, H.T. Li, H. Xu, H.M. Li, S.J. Guo, *Appl. Catal. B-Environ.* 181 (2016) 260–269.
- [17] N.N. Chai, H.X. Wang, C.X. Hu, Q. Wang, H.L. Zhang, *J. Mater. Chem. A* 3 (2015) 16613–16620.
- [18] X.C. Pang, Y.J. He, J.H. Jung, Z.Q. Lin, *Science* 353 (2016) 1268–1272.
- [19] H. Sun, J. Deng, L.B. Qiu, X. Fang, H.S. Peng, *Energy Environ. Sci.* 8 (2015) 1139–1159.
- [20] X.Q. An, J.C. Yu, Y. Wang, Y.M. Hu, X.L. Yu, G.J. Zhang, *J. Mater. Chem.* 22 (2012) 8525–8531.
- [21] M.Z. Ge, C.Y. Cao, J.Y. Huang, S.H. Li, Z. Chen, K.Q. Zhang, S.S. Al-Deyab, Y.K. Lai, *J. Mater. Chem. A* 4 (2016) 6772–6801.
- [22] M. Law, L.E. Greene, J.C. Johnson, R. Saykally, P.D. Yang, *Nat. Mater.* 4 (2005) 455–459.
- [23] P.M. Rao, L.L. Cai, C. Liu, I.S. Cho, C.H. Lee, J.M. Weisse, P.D. Yang, X.L. Zheng, *Nano Lett.* 14 (2014) 1099–1105.
- [24] W.N. Shi, X.F. Zhang, J. Brillet, D.K. Huang, M. Li, M.K. Wang, Y. Shen, *Carbon* 105 (2016) 387–393.
- [25] P.J. Yang, J.H. Zhao, J. Wang, B.Y. Cao, L. Li, Z.P. Zhu, *J. Mater. Chem. A* 3 (2015) 8256–8259.
- [26] L.J. Zhang, S. Li, B.K. Liu, D. Wang, T.F. Xie, *ACS Catal.* 4 (2014) 3724–3729.
- [27] J. Jin, J.G. Yu, D.P. Guo, C. Cui, W.K. Ho, *Small* 11 (2015) 5262–5271.
- [28] H. Ming, Z. Ma, Y. Liu, K.M. Pan, H. Yu, F. Wang, Z.H. Kang, *Dalton. Trans.* 41 (2012) 9526–9531.
- [29] J. Zhang, X.Y. Zhang, S.S. Dong, X. Zhou, S.S. Dong, *J. Photochem. Photobiol. A: Chem.* 325 (2016) 104–110.
- [30] H.T. Li, Z.H. Kang, Y. Liu, S.T. Lee, *J. Mater. Chem.* 22 (2012) 24230–24253.
- [31] X.J. Yu, J.J. Liu, Y.C. Yu, S.L. Zuo, B.S. Li, *Carbon* 68 (2014) 718–724.
- [32] S.Y. Zhao, C.X. Li, L.P. Wang, N.Y. Liu, S. Qiao, B.B. Liu, H. Huang, Y. Liu, Z.H. Kang, *Carbon* 99 (2016) 599–606.
- [33] J. Di, J.X. Xia, M.X. Ji, L. Xu, S. Yin, Z.G. Chen, H.M. Li, *J. Mater. Chem. A* 4 (2016) 5051–5061.
- [34] C.Y. Wang, X. Zhang, X.N. Song, W.K. Wang, H.Q. Yu, *ACS Appl. Mater. Interfaces* 8 (2016) 5320–5326.
- [35] A.Y. Zhang, W.K. Wang, D.N. Pei, H.Q. Yu, *Water. Res.* 92 (2016) 78–86.
- [36] H.J. Li, W.G. Tu, Y. Zhou, Z.G. Zou, *Adv. Sci.* 3 (2016).